

!YOUR TITLE ALL CAPS!

By Joel N. Johnson

A Dissertation

Submitted in Partial Fulfillment

of the Requirements for the Degree of

Doctor of Philosophy

in Applied Physics and Materials Science

Northern Arizona University

!Month YYYY!

Ryan O. Behunin, Ph.D., Co-Chair

John G. Gibbs, Ph.D., Co-Chair

Inès Montaña, Ph.D.

Jennifer S. Martinez, Ph.D.

Table of Contents

List of Tables	iv
List of Figures	v
Dedication	vii
Preface	ix
1 Introduction	1
1.1 Section 1	1
2 Manuscript I: Laser cooling of traveling wave phonons in an optical fiber	3
2.1 Abstract	3
2.2 Introduction	4
2.3 Laser cooling of traveling wave phonons	6
2.4 Methods & Results	8
2.5 Conclusions	10
2.6 Acknowledgements	11
3 Manuscript II: A coherently stimulated phonon spectrometer	13
3.1 Abstract	13
3.2 Introduction	13
3.2.1 Theory of CABS	13
3.2.2 Phase-matching at short lengths	13
3.3 Methods	13
3.3.1 Theory of CABS	13
3.3.2 Phase-matching bandwidth	14
3.4 Results	14
3.4.1 Design of instrument	14
3.4.2 From fiber-coupled to millimeter-scale bulk	14
3.4.3 Relaxation of Phase-matching conditions	14
3.5 Discussion	14
3.6 Acknowledgements	14
3.7 Appendix	14
3.7.1 Equal contribution of P, S, Pr	14
4 Manuscript III: Brillouin-induced Raman modes	15
4.1 Abstract	15
4.2 Introduction	15
5 Manuscript IV: Nanoscale Brillouin scattering	17
5.1 Abstract	17
5.2 Introduction	17
6 Discussion & Conclusion	19

Acronyms	21
A Supplementary Information for Chapter 2: Manuscript I	23
A.1 Mean-field analysis of Brillouin cooling	23
A.1.1 Envelope analysis of cooling dynamics, and validity of the mean-field model	26
A.1.2 Separation of time scales required for cooling of travelling wave phonons	28
A.2 Pump-probe theory	28
A.3 Brillouin gain simulations	29
References	31

List of Tables

4.1	Table caption.	16
5.1	Table caption.	18
A.1	Parameters used in simulations of spontaneous Brillouin scattering spectra.	30

List of Figures

- 2.1 Illustration of (a) geometry and scattering processes in a liquid-core optical fiber (LCOF), (b) cooling signatures in spontaneous light scattering spectra, and simulated (c) optical and (d) mechanical modes. Simulations (c) and (d) plot the magnitudes of the electric and displacement fields respectively. 5
- 2.2 (a) Heterodyne spectroscopy apparatus for measuring power dependence of spontaneous Brillouin spectra shown in (b). Lorentzian fits to spectra in (b) reveal signatures of Brillouin cooling through (c) power-dependent linewidths and (d) sub- and super-linear growth of the power spectra peaks. The lines in (c) are obtained through a constrained fit using Eq. 2.5 providing an estimated Brillouin gain of 2.3 (Wm)^{-1} . Theory in (d) obtained using the fitted value of G_B , Eq. (2.6) and the measured spectra heights at 4.1 mW (see Appendix A).(e) Comparison between measured and simulated light scattering spectra (see Appendix C). Here, EDFA stands for Erbium doped fiber amplifier, BPF is a tunable band-pass filter, and VOA is variable optical attenuator. 6
- 2.3 Pump-probe measurements of Brillouin cooling. (a) Pump-probe spectrometer. Orthogonally polarized pump and fixed-power probe light are combined and sent into the sample using a polarizing beam splitter (PBS). Backscattered pump and probe light exit distinct ports of the PBS, and anti-Stokes sideband is isolated using a circulator and tunable bandpass filter (BPF). Orthogonally polarized pump and probe beams (b) and (c) couple to the same band of phonons. The scattered probe can be isolated from the scattered pump using a PBS. (d) Backscattered anti-Stokes power spectra for the probe plotted for various pump powers. For clarity the data is averaged over 1.67 MHz bins. (e) Comparison of measured anti-Stokes spectra and the power spectrum predicted by mean-field theory (see Appendix B). 9

Dedication

Lorem ipsum dolor sit amet, consectetur adipiscing elit. Ut purus elit, vestibulum ut, placerat ac, adipiscing vitae, felis. Curabitur dictum gravida mauris. Nam arcu libero, nonummy eget, consectetur id, vulputate a, magna. Donec vehicula augue eu neque. Pellentesque habitant morbi tristique senectus et netus et malesuada fames ac turpis egestas. Mauris ut leo. Cras viverra metus rhoncus sem. Nulla et lectus vestibulum urna fringilla ultrices. Phasellus eu tellus sit amet tortor gravida placerat. Integer sapien est, iaculis in, pretium quis, viverra ac, nunc. Praesent eget sem vel leo ultrices bibendum. Aenean faucibus. Morbi dolor nulla, malesuada eu, pulvinar at, mollis ac, nulla. Curabitur auctor semper nulla. Donec varius orci eget risus. Duis nibh mi, congue eu, accumsan eleifend, sagittis quis, diam. Duis eget orci sit amet orci dignissim rutrum.

Preface

Lorem ipsum dolor sit amet, consectetur adipiscing elit. Ut purus elit, vestibulum ut, placerat ac, adipiscing vitae, felis. Curabitur dictum gravida mauris. Nam arcu libero, nonummy eget, consectetur id, vulputate a, magna. Donec vehicula augue eu neque. Pellentesque habitant morbi tristique senectus et netus et malesuada fames ac turpis egestas. Mauris ut leo. Cras viverra metus rhoncus sem. Nulla et lectus vestibulum urna fringilla ultrices. Phasellus eu tellus sit amet tortor gravida placerat. Integer sapien est, iaculis in, pretium quis, viverra ac, nunc. Praesent eget sem vel leo ultrices bibendum. Aenean faucibus. Morbi dolor nulla, malesuada eu, pulvinar at, mollis ac, nulla. Curabitur auctor semper nulla. Donec varius orci eget risus. Duis nibh mi, congue eu, accumsan eleifend, sagittis quis, diam. Duis eget orci sit amet orci dignissim rutrum.

Chapter 1

Introduction

This is an inline citation, Boyd (2020). This is a parenthetical citation (Boyd, 2020). This is a figure reference (Figure 2.1). This is a section reference §1.1. This is a chapter reference with chapter spelled out: chapter 2. This is an acronym definition American Geophysical Union (AGU). This is the second time I use the acronym in this section AGU. This is if I want to spell out the full acronym again American Geophysical Union (AGU). Define new acronyms in the acronyms.tex file.

1.1 Section 1

Lorem ipsum dolor sit amet, consectetur adipiscing elit. Ut purus elit, vestibulum ut, placerat ac, adipiscing vitae, felis. Curabitur dictum gravida mauris. Nam arcu libero, nonummy eget, consectetur id, vulputate a, magna. Donec vehicula augue eu neque. Pellentesque habitant morbi tristique senectus et netus et malesuada fames ac turpis egestas. Mauris ut leo. Cras viverra metus rhoncus sem. Nulla et lectus vestibulum urna fringilla ultrices. Phasellus eu tellus sit amet tortor gravida placerat. Integer sapien est, iaculis in, pretium quis, viverra ac, nunc. Praesent eget sem vel leo ultrices bibendum. Aenean faucibus. Morbi dolor nulla, malesuada eu, pulvinar at, mollis ac, nulla. Curabitur auctor semper nulla. Donec varius orci eget risus. Duis nibh mi, congue eu, accumsan eleifend, sagittis quis, diam. Duis eget orci sit amet orci dignissim rutrum.

Chapter 2

Manuscript I: Laser cooling of traveling wave phonons in an optical fiber

Joel N. Johnson^{1,2}, Danielle R. Haverkamp^{1,2}, Yi-Hsin Ou³, Khanh Kieu³, Nils T. Otterstrom⁴, Peter T. Rakich⁵, Ryan O. Behunin^{1,2}

This is the Accepted Manuscript version of an article accepted for publication in Physical Review Applied. Wiley Inc is not responsible for any errors or omissions in this version of the manuscript or any version derived from it. The Version of Record is available online at <https://doi.org/>.

2.1 Abstract

In recent years, optical control of mechanical oscillators has emerged as a critical tool for everything from information processing to laser cooling. While traditional forms of optomechanical cooling utilize systems comprising discrete optical and mechanical modes, it has recently been shown that cooling can be achieved in a chip-based system that possesses a continuum of modes. Through Brillouin-mediated phonon photon interactions, cooling of a band of traveling acoustic waves can occur when anti-Stokes scattered photons exit the system more rapidly than the relaxation rate of the mechanical waves, to a degree determined by the acousto-optic coupling. Here, we demonstrate that a continuum of travelingwave phonons can be cooled within an optical fiber, extending this physics to macroscopic length scales. Leveraging the large acousto-optic coupling permitted within a liquid-core optical fiber, heterodyne spectroscopy reveals power-dependent changes in spontaneous-Brillouin-scattering spectra that indicate a reduction of the thermal phonon population by 21 K using 120 mW of injected laser power. These results provide alternative ways to manipulate phonon populations that could enable acousto-optic applications Q2 with reduced noise or provide ways to control traveling-wave phonons at the quantum level.

¹ Department of Applied Physics and Materials Science, Northern Arizona University, Flagstaff, AZ 86011, USA

² Center for Materials Interfaces in Research and Applications, Flagstaff, AZ 86011, USA

³ College of Optical Sciences, University of Arizona, 1630 E University Blvd, Tucson, AZ 85721, USA

⁴ Sandia National Laboratory, 1515 Eubank Blvd SE, Albuquerque, NM 87123, USA

⁵ Department of Applied Physics, Yale University, New Haven, CT 06520, USA

2.2 Introduction

Laser cooling has brought about a revolution in atomic, molecular, and optical (AMO) physics, permitting exquisite control of the motion of ions, atoms, and molecules, precision measurements of time, and the creation of alternative states of matter (Hänsch & Schawlow, 1975; Ashkin, 1978; Wineland et al., 1978; Phillips & Metcalf, 1982; Anderson et al., 1995; Davis et al., 1995; Ludlow et al., 2015; Epstein et al., 1995; Sheik-Bahae & Epstein, 2007). Beyond these AMO applications, laser cooling has led to impressive developments in solid-state systems where optical refrigeration in rare earth doped glasses is rapidly approaching cryogenic operation, and sideband cooling of individual mesoscopic mechanical oscillators has opened new windows to the foundations of physics and enabled the generation of novel quantum states (Chan et al., 2011; Marshall et al., 2003; Hong et al., 2017; Aspelmeyer et al., 2014).

Laser cooling of mechanical oscillators conventionally utilize an optical cavity with a movable mirror where radiation pressure mediates a parametric coupling between cavity resonance and a discrete phononic mode (Aspelmeyer et al., 2014). This configuration is critical to optical sideband cooling, where drive laser photons, with frequencies red-detuned from an optical resonance, can preferentially blue-shift by phonon scattering, rapidly exit the system, and lower the effective phonon occupancy (Aspelmeyer et al., 2014). While optomechanical cooling of traveling wave phonons has been achieved in whispering gallery mode resonators that support discrete optical and mechanical modes (Bahl et al., 2012), surprisingly, this form of anti-Stokes cooling can occur in continuous systems—without optical or mechanical resonances (Otterstrom et al., 2018). Otterstrom *et al.* showed that cooling of a continuous band of phonon modes can be achieved when injected laser light scatters through an anti-Stokes process from traveling wave phonons and exits the system more rapidly than the phonon bath returns to thermal equilibrium. Because distinct traveling phonon modes mediate Stokes and anti-Stokes scattering in a continuous system, it is possible to cool a selected band of phonons as any simultaneous Stokes ‘heating’ will change the population of a distinct mode. This form of cooling simultaneously requires substantial light-sound couplings, to enable efficient scattering, and phonon lifetimes exceeding the transit time for light through the waveguide. Owing to these stringent requirements, optomechanical cooling in continuous systems has only been observed in silicon waveguides engineered to have large Brillouin coupling and short \sim cm lengths. While the realization of this physics within optical fibers may be attractive for low-noise signal processing, high-coherence lasers, high-fidelity optical squeezing, and variable bandwidth forms of all-optical slow-light generation, demonstration of cooling of travelling wave phonons in fibers has remained elusive (Shin et al., 2015; Shelby et al., 1986; Okawachi et al., 2005).

Here, we demonstrate cooling of a continuum of phonon modes in optical fiber for the first time. Through spontaneous Brillouin scattering in a 1m long CS₂-filled liquid-core optical fiber, we achieve cooling (i.e.,

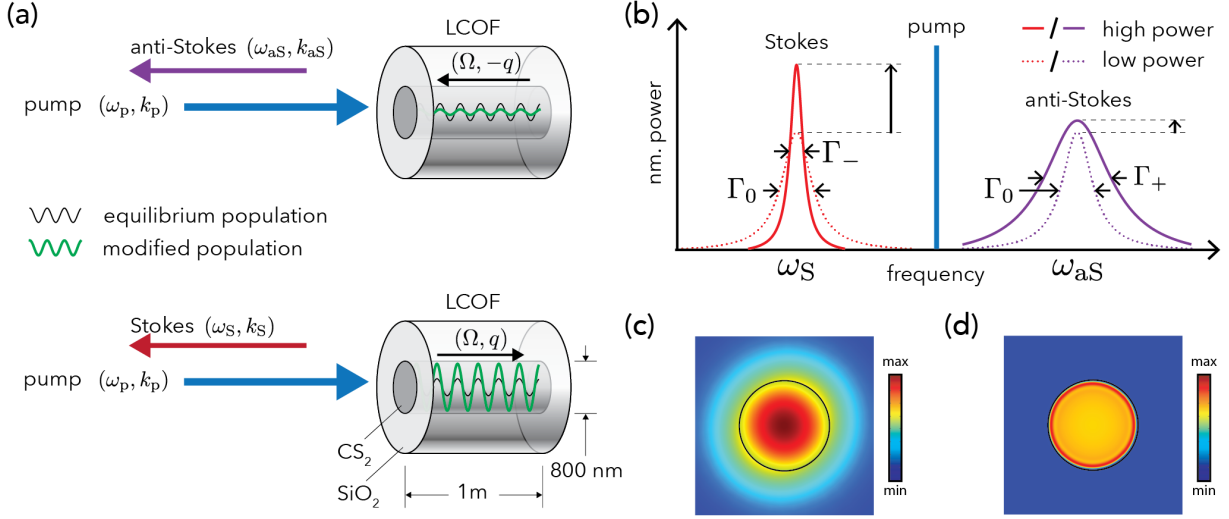


Figure 2.1: Illustration of (a) geometry and scattering processes in a liquid-core optical fiber (LCOF), (b) cooling signatures in spontaneous light scattering spectra, and simulated (c) optical and (d) mechanical modes. Simulations (c) and (d) plot the magnitudes of the electric and displacement fields respectively.

change in temperature) of $\sim 21\text{K}$ from room temperature for a band of anti-Stokes phonons. These dynamics are made possible by the unique features of this fiber system (Fig. 2.1)(Kieu et al., 2013, 2014; Behunin et al., 2019). The large refractive index and small sound speed of CS₂ enable simultaneous guidance and tight co-confinement of light and sound (Fig. 2.1c & d) within small diameter silica capillaries. This tight acousto-optic overlap, combined with the large electrostrictive coupling made possible within CS₂ (Boyd, 2020) permit large light-sound interactions which can be leveraged for optomechanical cooling in a continuous system.

Using heterodyne spectroscopy, we show how spontaneously scattered power spectra evolve with pump power. These spectra reveal the signatures of cooling, showing changes in the phonon dissipation rate and nonlinear dependence on the pump power. To confirm depletion of thermal phonons, we perform a form of pump-probe spontaneous Brillouin scattering where changes in the phonon population can be directly probed. This pump-probe technique leverages a unique property of Brillouin scattering, permitting two orthogonal polarizations of light to couple to the same band of phonons. Using this feature an intense pump can be used to cool the phonon modes while a weak probe laser in an orthogonal polarization, that can be isolated from the pump, measures the phonon population. With fixed probe powers, these results show that the power of anti-Stokes scattered probe light decreases as the pump power is increased, indicating that the thermal population of the anti-Stokes phonons has been reduced in a manner consistent with theory. With the long lengths and power-handling capabilities of optical fibers, combined with recent theoretical developments, these results may enable new low-noise fiber applications, ground state cooling of bands of

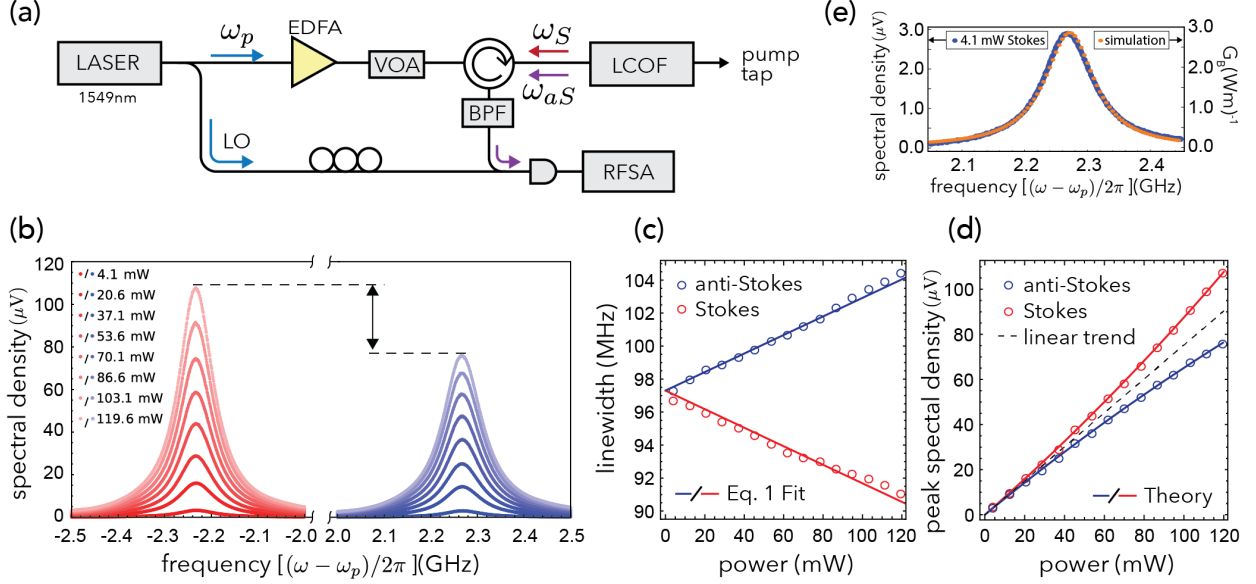


Figure 2.2: (a) Heterodyne spectroscopy apparatus for measuring power dependence of spontaneous Brillouin spectra shown in (b). Lorentzian fits to spectra in (b) reveal signatures of Brillouin cooling through (c) power-dependent linewidths and (d) sub- and super-linear growth of the power spectra peaks. The lines in (c) are obtained through a constrained fit using Eq. 2.5 providing an estimated Brillouin gain of 2.3 (Wm)^{-1} . Theory in (d) obtained using the fitted value of G_B , Eq. (2.6) and the measured spectra heights at 4.1 mW (see Appendix A). (e) Comparison between measured and simulated light scattering spectra (see Appendix C). Here, EDFA stands for Erbium doped fiber amplifier, BPF is a tunable band-pass filter, and VOA is variable optical attenuator.

traveling phonon modes, and new forms of quantum state synthesis (Zhu & Stiller, 2022; Behunin & Rakich, 2023).

2.3 Laser cooling of traveling wave phonons

Laser cooling of traveling wave phonons occurs through anti-Stokes Brillouin scattering. During this process an incident pump photon annihilates a counter-propagating phonon, blue-shifts to higher energy, and rapidly exits the system (Fig. 2.1a). The frequencies and wavevectors of the participating guided waves satisfy the following phase-matching conditions

$$\omega_p + \Omega = \omega_{aS} \quad (2.1)$$

$$k_p - q = -k_{aS} \quad (2.2)$$

where the angular frequencies (wavevectors) for the pump, phonon, and anti-Stokes modes are given by ω_p , Ω , and ω_{aS} (k_p , $-q$, and $-k_{aS}$). Here, the propagation direction of the mode is denoted by the sign of the

wavevector. For a selected pump frequency, the dispersion relations, for both light and mechanical waves, and Eqs. (2.1)& (2.2) can be used to find the frequency of the traveling wave phonon that participates in anti-Stokes Brillouin scattering

$$\Omega \approx \frac{2nv}{c}\omega_p \quad (2.3)$$

where n is the refractive index, v is the speed of sound, and c is the speed of light in vacuum. It is important to note that Stokes scattering will also occur within the system, tending to increase the population of phased-matched phonons that co-propagate with the pump (Fig. 2.1 a). As a result, ‘heating’ of the phonons participating in the Stokes process and cooling of the distinct counter-propagating phonon mode mediating anti-Stokes scattering will proceed simultaneously. While cooling of a band of traveling wave phonons can be achieved and independently detected, unless Stokes scattering is suppressed, the system as a whole will not be cooled.

In order for cooling to occur, the mechanical degrees of freedom must return to thermal equilibrium more slowly than the anti-Stokes photons exit the system. A mean-field analysis of these dynamics, described in Appendix A, shows that these conditions require $4v_g/L > \Gamma_0$, where v_g is the optical group velocity, L is the system length and Γ_0 is the mechanical dissipation rate (Otterstrom et al., 2018), conditions met by the system considered here (Fig. 2.1(a)) with $4v_g/L \approx 0.82$ GHz and $\Gamma_0 \approx 0.61$ GHz. While these disparate optical and mechanical timescales allow the phonon population to be driven out of thermal equilibrium, the degree of cooling requires a relatively large single pass Brillouin gain $G \equiv G_B P_p L$ where G_B is the Brillouin gain coefficient [$\text{m}^{-1}\text{W}^{-1}$] and P_p is the pump power (Boyd, 2020), yielding a fractional temperature $\Delta T/T_0$ change given approximately by

$$\frac{\Delta T}{T_0} \approx \frac{G}{G+4} \quad (2.4)$$

where T_0 is the equilibrium temperature (Otterstrom et al., 2018). Therefore, we must balance competing requirements, maximizing the single-pass gain while minimizing the light travel time across the fiber to achieve efficient cooling. Although the mean-field optical decay rate is marginally greater than the phonon decay rate, analysis of the coupled envelope dynamics shows that the key conclusions of the mean-field analysis remain valid in the limit of small single-pass gains explored here (see Appendix A.1).

Cooling of traveling wave phonons can be identified by power-dependent changes in the width and height of spontaneous light scattering spectra, revealing the phonon band temperature and dissipation rate (Fig. 2.1b). While for low power ($G \ll 1$) the spectrum height increases linearly with pump power, these increases begin to saturate (grow more rapidly) for the anti-Stokes (Stokes) spectrum as the single pass gain approaches

one and the phonon population is depleted (increased). Consequently, the anti-Stokes (Stokes) spectrum height grows sub-linearly (super-linearly), depending on both the pump power and the phonon population (Figs. 2.1b & 2.2d). Owing to additional decay (amplification) channels opened by spontaneous anti-Stokes (Stokes) Brillouin scattering, the phonon dissipation rate increases (decreases) with pump power according to

$$\Gamma_{\pm} \approx \Gamma_0 \left(1 \pm \frac{1}{4}G \right) \quad (2.5)$$

where the upper (+) sign indicates an increase in the anti-Stokes phonon decay rate and the lower (-) sign quantifies how the Stokes spectrum narrows (Otterstrom et al., 2018). Interestingly, the Brillouin nonlinearity increases the group velocity of the anti-Stokes photons (Gonzalez-Herraez et al., 2005). As a result, the conditions for cooling can be met even as the phonon decay rate increases, i.e., $4v_{g,eff}/L > \Gamma_+$ (see Appendix Sec. A) As a consequence of these altered decay rates, detailed balance for thermal equilibrium is broken, reducing (or increasing) the effective population of the anti-Stokes (Stokes) phonons $n_{eff}^+(n_{eff}^-)$ described by

$$n_{eff}^{\pm} \approx \frac{\Gamma_0}{\Gamma_{\pm}} n_{th}, \quad (2.6)$$

where $n_{th} \approx 2700$, given by the Bose distribution, is the occupation number for the relevant phonons in our liquid-core optical fiber (LCOF) in thermal equilibrium (Otterstrom et al., 2018). See Appendix A for more details of the mean-field analysis of the nonlinear optics in this system.

To demonstrate this physics, we utilize a 1m long CS₂-filled silica capillary (Fig. 2.1), possessing an array of properties that are ideal for laser cooling of traveling wave phonons. The materials properties and geometry of this liquid-filled capillary permit guided optical (single-mode at 1.55 μm) (Fig. 2.1c) and acoustic waves (Fig. 2.1d) within the 800nm diameter fiber core and enable large Brillouin gain (see Tab. I in App. C for more details). Furthermore, macroscopic meter-scale lengths make large single-pass gain accessible at modest sub-Watt powers. See Refs. (Kieu et al., 2013, 2014; Behunin et al., 2019) for details on Brillouin scattering in LCOFs.

2.4 Methods & Results

We measure Brillouin cooling in this LCOF using the apparatus shown in Fig. 2.2a. The output of a laser is split in two, a variable power arm is injected into the sample for Brillouin cooling, and a fixed-power arm is used to synthesize a local oscillator (LO) for heterodyne detection. Spontaneously backscattered light is filtered, to remove stray pump light and isolate the anti-Stokes (or Stokes) sideband, photomixed with the LO on a high-speed receiver, and detected on a radio-frequency spectrum analyzer (RFSa) as a function of

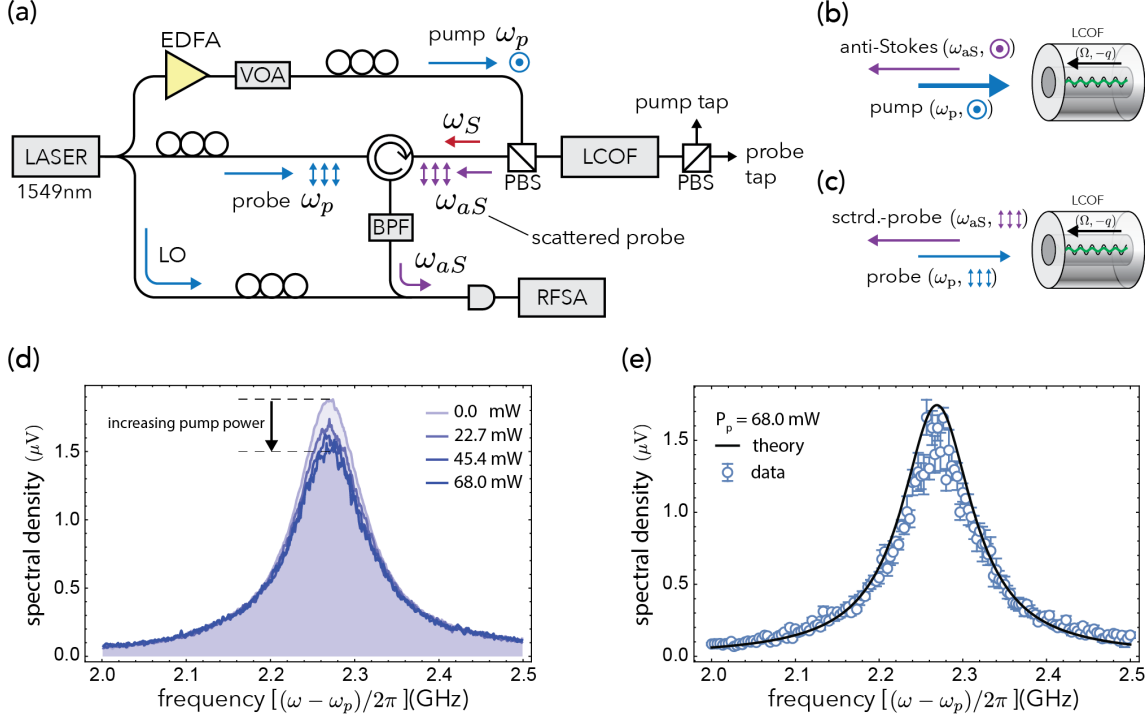


Figure 2.3: Pump-probe measurements of Brillouin cooling. (a) Pump-probe spectrometer. Orthogonally polarized pump and fixed-power probe light are combined and sent into the sample using a polarizing beam splitter (PBS). Backscattered pump and probe light exit distinct ports of the PBS, and anti-Stokes sideband is isolated using a circulator and tunable bandpass filter (BPF). Orthogonally polarized pump and probe beams (b) and (c) couple to the same band of phonons. The scattered probe can be isolated from the scattered pump using a PBS. (d) Backscattered anti-Stokes power spectra for the probe plotted for various pump powers. For clarity the data is averaged over 1.67 MHz bins. (e) Comparison of measured anti-Stokes spectra and the power spectrum predicted by mean-field theory (see Appendix B).

pump power. These measurements yield spontaneous Brillouin scattering spectra of the type shown in Fig. 2.2b.

The data displayed in Fig. 2.2 exhibit key signatures of Brillouin cooling. With increasing pump power, the linewidth of the anti-Stokes spectrum increases and the scattered anti-Stokes power increases sub-linearly (Fig. 2.2c & d). The extracted linewidths of the Stokes and anti-Stokes spectra exhibit the power dependence described by Eq. (2.5), yielding a Brillouin gain coefficient $G_B \sim 2.3(\text{Wm})^{-1}$, qualitatively described by finite-element simulations shown in Fig. 2.2e predicting $G_B \approx 2.9 (\text{Wm})^{-1}$. Using Eq. (2.4), these measurements show that the temperature of the band of traveling anti-Stokes phonons has been reduced by 21K from room temperature for 120mW of pump power.

The apparatus and data shown in Fig. 2.2 directly demonstrate the signatures of laser cooling of a continuous band of phonons. However, in these measurements, the amplitude of the power spectrum is proportional to the product of phonon population and the pump power. To directly detect changes to the

phonon population, we utilize a form of pump-probe spectroscopy shown in Fig. 2.3. In contrast with the heterodyne measurements depicted in Fig. 2.2, the output of a laser is divided into a variable power pump, and a fixed power probe. Orthogonally polarized pump and probe beams are combined using a polarizing beam splitter (PBS) and sent into the LCOF where they interact with the same phonon mode (Fig. 2.3 b & c). Owing to this polarization multiplexing, spontaneously back-scattered probe light is separated from the backscattered pump by the PBS, filtered, and photomixed with the LO for heterodyne detection, yielding the spectra shown in Fig. 2.3d. Consistent with the depopulation of phonons, these results show a decrease in the anti-Stokes scattering rate with increasing in pump power. Furthermore, Fig. 2.3c shows that these spectra are well-described by a simple model of the pump-probe dynamics with parameters obtained from independent measurements shown in Fig. 2.2. See Appendix B for further details of the pump-probe theory.

2.5 Conclusions

We have demonstrated laser cooling of travelling wave phonons in an optical fiber for the first time. Using spontaneous Brillouin light scattering spectroscopy of a CS₂-filled LCOF, we probe the populations of travelling wave phonons, revealing power-dependent changes in the phonon dynamics consistent with a mean-field model and finite-element simulations. Key to accessing this regime of light matter interactions is the large acousto-optic coupling and short length of our sample, where pump photons readily scatter from counter-propagating phonons and rapidly exit the fiber before the phonons can return to thermal equilibrium. The combination of these properties enables 21K of phonon cooling for 120mW of pump power.

Building on these results, drastic enhancements in our ability to cool traveling wave phonons may be achievable with changes in the fiber geometry and material. With larger core diameters, the Brillouin gain can be dramatically increased through improved acousto-optic overlap as well as through increased optical intensity. Working toward the limit of single-mode operation (for 1.55 μm optical wavelengths), finite-element simulations predict Brillouin gains of $\sim 11 \text{ (Wm)}^{-1}$ for a LCOF with a 1.6 μm core diameter, exceeding the acousto-optic coupling in our LCOF by nearly a factor of five. Under the same experimental conditions as this study, such a fiber could achieve 119 K of cooling for 250 mW of pump power, approaching cryogenic temperatures. Alternatively, chalcogenide glass fibers can be used to achieve much large Brillouin gains (Abedin, 2005). For example, 6 μm core diameter As₂Se₃ fibers achieve bulk Brillouin gain of $g_B = 6.2 \times 10^{-9} \text{ m/W}$, translating to an approximate Brillouin gain coefficient of $G_B \sim 159 \text{ (Wm)}^{-1}$. In such a system, Eq. (2.4) shows that 100K of cooling can be achieved in a 1 m fiber with 13mW of pump power.

As thermal noise produced by traveling wave phonons is a critical limitation in a variety of fiber-based applications including information processing, lasers, and quantum optics experiments, these results may

inspire new ways to achieve improved performance. The techniques demonstrated in this paper may be used to create new Brillouin laser technologies with superb stability (Behunin et al., 2018; Li et al., 2012), reduce backscatter produced by spontaneous Brillouin scattering in fiber optic communications, suppress guided acoustic wave modulation of quantum optical signals, or enable all-optical delay lines with tunable bandwidth (Okawachi et al., 2005).

2.6 Acknowledgements

J. J. and R. B. acknowledge funding from NSF Award No. 2145724. This article has been authored by an employee of National Technology & Engineering Solutions of Sandia, LLC under Contract No. DE-NA0003525 with the U.S. Department of Energy (DOE). The employee owns all right, title and interest in and to the article and is solely responsible for its contents. The United States Government retains and the publisher, by accepting the article for publication, acknowledges that the United States Government retains a non-exclusive, paid-up, irrevocable, world-wide license to publish or reproduce the published form of this article or allow others to do so, for United States Government purposes. The DOE will provide public access to these results of federally sponsored research in accordance with the DOE Public Access Plan <https://www.energy.gov/downloads/doe-public-access-plan>.

Chapter 3

Manuscript II: A coherently stimulated phonon spectrometer

Joel N. Johnson^{1,2}, Nils T. Otterstrom³, Peter T. Rakich⁴, Ryan O. Behunin^{1,2}

This is the Accepted Manuscript version of an article accepted for publication in Nature Photonics. Wiley Inc is not responsible for any errors or omissions in this version of the manuscript or any version derived from it. The Version of Record is available online at <https://doi.org/>.

3.1 Abstract

3.2 Introduction

State of brillouin microscopy Applications and usefulness Challenges: selection of backscattered signal conflated with Stokes field phase-matching requires probe wavelength to be exactly that of Stokes Wouldn't it be nice if we could break free of strict phase-matching requirements, therefore perfectly isolating the signal In this work

3.2.1 Theory of CABS

description of physics with scattered power equation

3.2.2 Phase-matching at short lengths

phase-matching bandwidth description with equation

3.3 Methods

3.3.1 Theory of CABS

full CABS theory arriving at scattered power

¹ Department of Applied Physics and Materials Science, Northern Arizona University, Flagstaff, AZ 86011, USA

² Center for Materials Interfaces in Research and Applications, Flagstaff, AZ 86011, USA

³ Sandia National Laboratory, 1515 Eubank Blvd SE, Albuquerque, NM 87123, USA

⁴ Department of Applied Physics, Yale University, New Haven, CT 06520, USA

3.3.2 Phase-matching bandwidth

phase-matching bandwidth theory

3.4 Results

3.4.1 Design of instrument

description of design figure: instrument apparatus design sensitivity measurements

3.4.2 From fiber-coupled to millimeter-scale bulk

figure: demonstration measurements 1mm uhna3 fiber 1mm CS2 bulk comparison to stimulated brillouin and spontaneous brillouin?

3.4.3 Relaxation of Phase-matching conditions

figure: phase-matching peak vs pump-probe separation 1cm uhna3, CS2 peak vs pump-probe separation 1mm uhna3, CS2

3.5 Discussion

3.6 Acknowledgements

3.7 Appendix

3.7.1 Equal contribution of P, S, Pr

figure: P, S, Pr equal contributors

Chapter 4

Manuscript III: Brillouin-induced Raman modes

4.1 Abstract

Nam dui ligula, fringilla a, euismod sodales, sollicitudin vel, wisi. Morbi auctor lorem non justo. Nam lacus libero, pretium at, lobortis vitae, ultricies et, tellus. Donec aliquet, tortor sed accumsan bibendum, erat ligula aliquet magna, vitae ornare odio metus a mi. Morbi ac orci et nisl hendrerit mollis. Suspendisse ut massa. Cras nec ante. Pellentesque a nulla. Cum sociis natoque penatibus et magnis dis parturient montes, nascetur ridiculus mus. Aliquam tincidunt urna. Nulla ullamcorper vestibulum turpis. Pellentesque cursus luctus mauris.

4.2 Introduction

Nam dui ligula, fringilla a, euismod sodales, sollicitudin vel, wisi. Morbi auctor lorem non justo. Nam lacus libero, pretium at, lobortis vitae, ultricies et, tellus. Donec aliquet, tortor sed accumsan bibendum, erat ligula aliquet magna, vitae ornare odio metus a mi. Morbi ac orci et nisl hendrerit mollis. Suspendisse ut massa. Cras nec ante. Pellentesque a nulla. Cum sociis natoque penatibus et magnis dis parturient montes, nascetur ridiculus mus. Aliquam tincidunt urna. Nulla ullamcorper vestibulum turpis. Pellentesque cursus luctus mauris.

Nam dui ligula, fringilla a, euismod sodales, sollicitudin vel, wisi. Morbi auctor lorem non justo. Nam lacus libero, pretium at, lobortis vitae, ultricies et, tellus. Donec aliquet, tortor sed accumsan bibendum, erat ligula aliquet magna, vitae ornare odio metus a mi. Morbi ac orci et nisl hendrerit mollis. Suspendisse ut massa. Cras nec ante. Pellentesque a nulla. Cum sociis natoque penatibus et magnis dis parturient montes, nascetur ridiculus mus. Aliquam tincidunt urna. Nulla ullamcorper vestibulum turpis. Pellentesque cursus luctus mauris.

Table 4.1: Table caption.

	Parameter	Value	Description
Lookup Variables	lat	-85°–85°	Latitude (35 bins in 5° increments)
	ALBEDO	0.05–0.225	Bolometric albedo (6 bins in 0.035 increments)
	SLOPE	0°–90°	Surface slope (19 bins in 5° increments)
	SLOAZI	0°–360°	Surface azimuth (19 bins in 20° increments)
	DELLS	4°	L_s step size (90 bins spanning 0°–360°)
Thermal Parameters	EMISS	0.96	Emissivity
	thick	0.05	Upper layer thickness [m]
	DENSITY	1100	Upper layer density [kg/m ³]
	DENS2	1800	Lower layer density [kg/m ³]
	lbound	18	Interior heat flow [mW/m ²]
	PhotoFunc	0.045/albedo	Photometric function (Keihm-style)
Temperature-dependent parameters	SphUp0/SphLo0	602.88098583	Specific heat capacity expressed as 4th-order polynomial ($c_0 + c_1 \cdot T + c_2 \cdot T^2 + c_3 \cdot T^3$)
	SphUp1/SphLo1	235.98988249	
	SphUp2/SphLo2	-29.59742178	
	SphUp3/SphLo3	-3.78707193	
	ConUp0	0.00133644	Upper layer conductivity expressed as 4th-order polynomial ($c_0 + c_1 \cdot T + c_2 \cdot T^2 + c_3 \cdot T^3$)
	ConUp1	0.00073150	
	ConUp2	0.00033250	
	ConUp3	0.00005038	
	ConLo0	0.00634807	Lower layer conductivity expressed as 4th-order polynomial ($c_0 + c_1 \cdot T + c_2 \cdot T^2 + c_3 \cdot T^3$)
	ConLo1	0.00347464	
	ConLo2	0.00157938	
	ConLo3	0.00023930	
Model Setup Parameters	body	Moon	Target body
	k.style	Moon	Conductivity style (Moon for airless bodies)
	LKofT	T	Temperature-dependent conductivity
	FLAY	0.01	First layer thickness [m]
	RLAY	1.3	Layer thickness multiplier
	N1	26	Number of layers
	N24	288	Timesteps per day (5 min steps)
	DJUL	0	Start date

Chapter 5

Manuscript IV: Nanoscale Brillouin scattering

5.1 Abstract

Nam dui ligula, fringilla a, euismod sodales, sollicitudin vel, wisi. Morbi auctor lorem non justo. Nam lacus libero, pretium at, lobortis vitae, ultricies et, tellus. Donec aliquet, tortor sed accumsan bibendum, erat ligula aliquet magna, vitae ornare odio metus a mi. Morbi ac orci et nisl hendrerit mollis. Suspendisse ut massa. Cras nec ante. Pellentesque a nulla. Cum sociis natoque penatibus et magnis dis parturient montes, nascetur ridiculus mus. Aliquam tincidunt urna. Nulla ullamcorper vestibulum turpis. Pellentesque cursus luctus mauris.

5.2 Introduction

Nam dui ligula, fringilla a, euismod sodales, sollicitudin vel, wisi. Morbi auctor lorem non justo. Nam lacus libero, pretium at, lobortis vitae, ultricies et, tellus. Donec aliquet, tortor sed accumsan bibendum, erat ligula aliquet magna, vitae ornare odio metus a mi. Morbi ac orci et nisl hendrerit mollis. Suspendisse ut massa. Cras nec ante. Pellentesque a nulla. Cum sociis natoque penatibus et magnis dis parturient montes, nascetur ridiculus mus. Aliquam tincidunt urna. Nulla ullamcorper vestibulum turpis. Pellentesque cursus luctus mauris.

Nam dui ligula, fringilla a, euismod sodales, sollicitudin vel, wisi. Morbi auctor lorem non justo. Nam lacus libero, pretium at, lobortis vitae, ultricies et, tellus. Donec aliquet, tortor sed accumsan bibendum, erat ligula aliquet magna, vitae ornare odio metus a mi. Morbi ac orci et nisl hendrerit mollis. Suspendisse ut massa. Cras nec ante. Pellentesque a nulla. Cum sociis natoque penatibus et magnis dis parturient montes, nascetur ridiculus mus. Aliquam tincidunt urna. Nulla ullamcorper vestibulum turpis. Pellentesque cursus luctus mauris.

Table 5.1: Table caption.

	Parameter	Value	Description
Lookup Variables	lat	-85°–85°	Latitude (35 bins in 5° increments)
	ALBEDO	0.05–0.225	Bolometric albedo (6 bins in 0.035 increments)
	SLOPE	0°–90°	Surface slope (19 bins in 5° increments)
	SLOAZI	0°–360°	Surface azimuth (19 bins in 20° increments)
	DELLS	4°	L_s step size (90 bins spanning 0°–360°)
Thermal Parameters	EMISS	0.96	Emissivity
	thick	0.05	Upper layer thickness [m]
	DENSITY	1100	Upper layer density [kg/m ³]
	DENS2	1800	Lower layer density [kg/m ³]
	lbound	18	Interior heat flow [mW/m ²]
	PhotoFunc	0.045/albedo	Photometric function (Keihm-style)
Temperature-dependent parameters	SphUp0/SphLo0	602.88098583	Specific heat capacity expressed as 4th-order polynomial ($c_0 + c_1 \cdot T + c_2 \cdot T^2 + c_3 \cdot T^3$)
	SphUp1/SphLo1	235.98988249	
	SphUp2/SphLo2	-29.59742178	
	SphUp3/SphLo3	-3.78707193	
	ConUp0	0.00133644	Upper layer conductivity expressed as 4th-order polynomial ($c_0 + c_1 \cdot T + c_2 \cdot T^2 + c_3 \cdot T^3$)
	ConUp1	0.00073150	
	ConUp2	0.00033250	
	ConUp3	0.00005038	
	ConLo0	0.00634807	Lower layer conductivity expressed as 4th-order polynomial ($c_0 + c_1 \cdot T + c_2 \cdot T^2 + c_3 \cdot T^3$)
	ConLo1	0.00347464	
	ConLo2	0.00157938	
	ConLo3	0.00023930	
Model Setup Parameters	body	Moon	Target body
	k.style	Moon	Conductivity style (Moon for airless bodies)
	LKofT	T	Temperature-dependent conductivity
	FLAY	0.01	First layer thickness [m]
	RLAY	1.3	Layer thickness multiplier
	N1	26	Number of layers
	N24	288	Timesteps per day (5 min steps)
	DJUL	0	Start date

Chapter 6

Discussion & Conclusion

Nam dui ligula, fringilla a, euismod sodales, sollicitudin vel, wisi. Morbi auctor lorem non justo. Nam lacus libero, pretium at, lobortis vitae, ultricies et, tellus. Donec aliquet, tortor sed accumsan bibendum, erat ligula aliquet magna, vitae ornare odio metus a mi. Morbi ac orci et nisl hendrerit mollis. Suspendisse ut massa. Cras nec ante. Pellentesque a nulla. Cum sociis natoque penatibus et magnis dis parturient montes, nascetur ridiculus mus. Aliquam tincidunt urna. Nulla ullamcorper vestibulum turpis. Pellentesque cursus luctus mauris.

Acronyms

AGU American Geophysical Union

AMO atomic, molecular, and optical

RFSA radio-frequency spectrum analyzer

LO local oscillator

BPF bandpass filter

PBS polarizing beam splitter

LCOF liquid-core optical fiber

Appendix A

Supplementary Information for Chapter 2: Manuscript I

A.1 Mean-field analysis of Brillouin cooling

The key features of Brillouin cooling can be understood from a mean-field analysis of the slowly-varying envelope equations. For an undepleted pump and ignoring the propagation of phonons, spontaneous Brillouin scattering can be described by the following coupled stochastic envelope equations

$$\dot{A}_S + v_g \partial_z A_S = -ig A_p B_S^\dagger \quad (\text{A.1})$$

$$\dot{B}_S + \frac{\Gamma_0}{2} B_S = -ig A_p A_S^\dagger + \xi_S \quad (\text{A.2})$$

$$\dot{A}_{aS} + v_g \partial_z A_{aS} = -ig A_p B_{aS} \quad (\text{A.3})$$

$$\dot{B}_{aS} + \frac{\Gamma_0}{2} B_{aS} = -ig A_{aS} A_p^\dagger + \xi_{aS} \quad (\text{A.4})$$

expressed in a frame rotating at the resonance frequency for each field Kharel et al. (2016). Here, A_S (A_{aS}) and B_S (B_{aS}) are the respective (right-moving) optical and mechanical envelopes for the Stokes (anti-Stokes) process, A_p is the envelope for a constant undepleted pump, g is the Brillouin coupling, and v_g is the optical group velocity. Thermal fluctuations of the mechanical field are modeled using the locally correlated white noise Langevin forces ξ_j ($j = S$ or aS) with correlation properties

$$\langle \xi_j(t, z) \xi_{j'}^\dagger(t', z') \rangle = \Gamma_0 (n_{th} + 1) \delta_{jj'} \delta(t - t') \delta(z - z') \quad (\text{A.5})$$

$$\langle \xi_j^\dagger(t, z) \xi_{j'}(t', z') \rangle = \Gamma_0 n_{th} \delta_{jj'} \delta(t - t') \delta(z - z') \quad (\text{A.6})$$

and Γ_0 is the mechanical dissipation rate. Put in terms of readily measurable quantities, the power in an optical mode is given by $P_{S/aS/p} = \hbar \omega_{S/aS/p} v_g A_{S/aS/p}^\dagger A_{S/aS/p}$ and the Brillouin gain can be expressed as

$$G_B = \frac{4|g|^2}{\hbar \omega_p v_g^2 \Gamma_0}. \quad (\text{A.7})$$

We define the mean fields for the respective optical and mechanical fields a_j and b_j as the average of the envelope over the length of the waveguide

$$a_j = \frac{1}{L} \int_0^L dz A_j(z) \quad (\text{A.8})$$

$$b_j = \frac{1}{L} \int_0^L dz B_j(z). \quad (\text{A.9})$$

The mean field equations can be obtained by averaging Eqs. (A.1)-(A.4) over the waveguide length, giving

$$\dot{a}_S + \frac{\gamma}{2} a_S = -ig A_p b_S^\dagger \quad (\text{A.10})$$

$$\dot{b}_S + \frac{\Gamma_0}{2} b_S = -ig A_p a_S^\dagger + \bar{\xi}_S \quad (\text{A.11})$$

$$\dot{a}_{aS} + \frac{\gamma}{2} a_{aS} = -ig A_p b_{aS} \quad (\text{A.12})$$

$$\dot{b}_{aS} + \frac{\Gamma_0}{2} b_{aS} = -ig a_{aS} A_p^\dagger + \bar{\xi}_{aS} \quad (\text{A.13})$$

where $\bar{\xi}_j$ is the spatial average of the Langevin force. Here, the mean-field optical decay rate $\gamma = 4v_g/L$ is obtained from the spatial average of the derivative terms, assuming $a_j \approx (A_j(L) + A_j(0))/2$ and using that the scattered optical fields vanish at the input face, i.e., $A_j(0) = 0$, according to

$$\begin{aligned} \frac{v_g}{L} \int_0^L dz \partial_z A_k(z) &= \frac{v_g}{L} (A_k(L) - A_k(0)) \\ &= \frac{v_g}{L} (A_k(L) + A_k(0) - 2A_k(0)) \\ &= \frac{2v_g}{L} a_k. \end{aligned} \quad (\text{A.14})$$

Next we analyze the mean field dynamics. When $\gamma > \Gamma_0$, the optical fields respond to changes in the phonon amplitude faster than the phonon changes, enabling a quasistatic solution to the optical field dynamics given by

$$\frac{\gamma}{2} a_S \approx -ig A_p b_S^\dagger \quad (\text{A.15})$$

$$\frac{\gamma}{2} a_{aS} \approx -ig A_p b_{aS}. \quad (\text{A.16})$$

Inserting Eq. (A.15) & (A.16) into Eqs. (A.11) & (A.13) we find the effective phonon dynamics given by

$$\dot{b}_S + \frac{1}{2}\Gamma_S b_S = \bar{\xi}_S \quad (\text{A.17})$$

$$\dot{b}_{aS} + \frac{1}{2}\Gamma_{aS} b_{aS} = \bar{\xi}_{aS} \quad (\text{A.18})$$

where $P_p = \hbar\omega_p v_g A_p^\dagger A_p$, Eq. (A.7) and Eq. (2) of the main text have been used. In addition, to changing the effective phonon dynamics, these results show that the power spectra for the optical fields are proportional to the phonon power spectrum,

$$S_S[\omega] = \frac{4|g|^2|A_p|^2}{\gamma^2} \int_{-\infty}^{\infty} d\tau e^{i\omega\tau} \langle b_S(t+\tau) b_S^\dagger(t) \rangle \quad (\text{A.19})$$

$$S_{aS}[\omega] = \frac{4|g|^2|A_p|^2}{\gamma^2} \int_{-\infty}^{\infty} d\tau e^{i\omega\tau} \langle b_{aS}^\dagger(t+\tau) b_{aS}(t) \rangle \quad (\text{A.20})$$

illustrating how the optical power spectra, defined by $S_j[\omega] = \int_{-\infty}^{\infty} d\tau \exp\{i\omega\tau\} \langle a_j^\dagger(t+\tau) a_j(t) \rangle$, permit a form of nonequilibrium phonon spectroscopy. Solving Eqs. (A.17) and using the correlation properties for the spatially averaged Langevin forces given by

$$\langle \bar{\xi}_j(t) \bar{\xi}_{j'}^\dagger(t') \rangle = \frac{1}{L} \Gamma_0 (n_{th} + 1) \delta_{jj'} \delta(t - t') \quad (\text{A.21})$$

$$\langle \bar{\xi}_j^\dagger(t) \bar{\xi}_{j'}(t') \rangle = \frac{1}{L} \Gamma_0 n_{th} \delta_{jj'} \delta(t - t'), \quad (\text{A.22})$$

we find

$$S_S[\omega] = \frac{\Gamma_0 G}{4v_g} \frac{\Gamma_0 n_{th}}{\Gamma_S} \frac{\Gamma_S}{\omega^2 + \Gamma_S^2/4} \quad (\text{A.23})$$

$$S_{aS}[\omega] = \frac{\Gamma_0 G}{4v_g} \frac{\Gamma_0 n_{th}}{\Gamma_{aS}} \frac{\Gamma_{aS}}{\omega^2 + \Gamma_{aS}^2/4}. \quad (\text{A.24})$$

The peak of the power spectrum (i.e., on resonance, or $\omega = 0$), used for the theory in Fig. 2e, is given by

$$S_S^{peak}[P_p] = \frac{n_{th}}{v_g} \frac{G B P_p L}{(1 - \frac{1}{4} G_B P_p L)^2} \quad (\text{A.25})$$

$$S_{aS}^{peak}[P_p] = \frac{n_{th}}{v_g} \frac{G_B P_p L}{(1 + \frac{1}{4} G_B P_p L)^2}. \quad (\text{A.26})$$

To account for the radio-frequency to electrical conversion, the peak of the power spectrum at the lowest

power ($P_0 = 4.1$ mW) is used to scale the theoretical curves to have units of μV

$$S_S^{peak,RF}[P_p] = \frac{S_S^{peak,RF}[P_0]}{G_B P_0 L} \frac{G_B P_p L}{(1 - \frac{1}{4} G_B P_p L)^2} \quad (\text{A.27})$$

$$S_{aS}^{peak,RF}[P_p] = \frac{S_{aS}^{peak,RF}[P_0]}{G_B P_0 L} \frac{G_B P_p L}{(1 + \frac{1}{4} G_B P_p L)^2}. \quad (\text{A.28})$$

A.1.1 Envelope analysis of cooling dynamics, and validity of the mean-field model

Here, we show that in the limit of small single-pass gain, the conclusions of the mean-field model agree with the full envelope dynamics.

In the Fourier domain, Eq. (A.4) can be readily solved and inserted in Eq. (A.3), giving

$$(\partial_z - i\Lambda)A_{aS}(\omega, z) = -\frac{1}{v_g} i g A_p \hat{B}_{aS}(\omega, z) \quad (\text{A.29})$$

where

$$\Lambda = \frac{1}{v_g} \left[\omega + i \frac{|g|^2 |A_p|^2}{-i\omega + \Gamma_0/2} \right], \quad (\text{A.30})$$

and

$$\hat{B}(\omega, z) = \frac{1}{-i\omega + \Gamma_0/2} \xi(\omega, z). \quad (\text{A.31})$$

Using Eqs. (A.6) and (A.31), the solution to Eq. (A.29) at the exit face of the fiber ($z = L$),

$$A_{aS}(\omega, L) = -i \frac{g A_p}{v_g} \int_0^L dz e^{i\Lambda(L-z)} \hat{B}(\omega, z), \quad (\text{A.32})$$

can be directly used to obtain the power spectrum of spontaneously scattered anti-Stokes light

$$\begin{aligned} S_{aS,env}[\omega] &\equiv \frac{\langle A_{aS}^\dagger(\omega, L) A_{aS}(\omega', L) \rangle}{2\pi \delta(\omega - \omega')} \\ &= \frac{n_{th}}{v_g} \left[1 - e^{-G(\omega)} \right] \end{aligned} \quad (\text{A.33})$$

where

$$G(\omega) = \frac{\Gamma^2/4}{\omega^2 + \Gamma^2/4} G. \quad (\text{A.34})$$

Noting that the power spectrum obtained directly from (A.3) is directly related to the effective phonon power spectrum $S_B[\omega]$

$$\begin{aligned} S_{aS,env}[\omega] &= \left| \frac{gA_p}{v_g} \right|^2 \int_0^L dz \int_0^L dz' e^{i\frac{\omega}{v_g}(z-z')} \frac{\langle B^\dagger(\omega, z) B(\omega', z') \rangle}{2\pi\delta(\omega - \omega')} \\ &= \left| \frac{gA_p}{v_g} \right|^2 S_B[\omega], \end{aligned} \quad (\text{A.35})$$

(note the power spectrum of B as opposed to \hat{B}) we identify the anti-Stokes phonon power spectrum including the effects of optomechanical cooling

$$S_B[\omega] = \frac{4n_{th}L}{G\Gamma_0} (1 - e^{-G(\omega)}). \quad (\text{A.36})$$

Using $S_B[\omega]$ we can calculate the effective thermal occupation of the anti-Stokes phonon mode

$$n_{eff,env} = \frac{1}{2\pi L} \int_{-\infty}^{\infty} d\omega S_B[\omega] \quad (\text{A.37})$$

$$= n_{th} e^{-G/2} (I_0(G/2) + I_1(G/2)) \quad (\text{A.38})$$

where the ω -integral can be expressed in terms of modified Bessel function I_0 and I_1 . Moreover, the full-width at half maximum $\Gamma_{aS,env}$ can be calculated from S_B using $S_B[\Gamma_{aS,env}/2] = S_B[0]/2$ giving effective anti-Stokes phonon decay rate derived from the envelope dynamics given by

$$\Gamma_{aS,env} = \Gamma_0 \left[\frac{G}{-\ln((1 + e^{-G})/2)} - 1 \right]^{1/2}. \quad (\text{A.39})$$

In the limit of small single-pass gain G , these results can be compared with the mean-field model, showing agreement to order G for the effective phonon decay rate and order G^2 for the effective thermal occupation

$$n_{eff} \approx n_{th} (1 - G/4 + G^2/16 - G^3/64 + \dots) \quad (\text{A.40})$$

$$n_{eff,env} \approx n_{th} (1 - G/4 + G^2/16 - 5G^3/384 + \dots) \quad (\text{A.41})$$

$$\Gamma_{aS} = \Gamma_0 (1 + G/4) \quad (\text{A.42})$$

$$\Gamma_{aS,env} \approx \Gamma_0 (1 + G/4 + G^2/32 + \dots). \quad (\text{A.43})$$

For the maximum single pass gain explored in this study $G < 0.3$, the results of the mean-field and envelope models agree to better than 0.25% in effective lifewidths and better than 0.007% in effective thermal occupation. The above analysis is similar for the Stokes process.

A.1.2 Separation of time scales required for cooling of travelling wave phonons

For cooling of travelling wave phonons to occur, anti-Stokes photons must exit the system more rapidly than it takes for the phonon to return to equilibrium, i.e., $4v_g/L > \Gamma_0$. While the optomechanical cooling dynamics leads to an increase in the phonon relaxation rate Γ_+ with pump power, as described by Eq. (2.5), we will show that a simultaneous increase in the anti-Stokes photon group velocity preserves the required separation of timescales. Noting that the effective anti-Stokes group velocity is given by

$$v_{g,eff} = \left(\frac{\partial \text{Re}[\Lambda]}{\partial \omega} \right)^{-1} \approx \left(\frac{1}{v_g} - \frac{G_B P_p}{\Gamma_0} \right)^{-1} \quad (\text{A.44})$$

where Λ is defined in Eq. (A.30) and it is assumed that ω is near resonance, i.e., $\omega \ll \Gamma_0$ Okawachi et al. (2005); Gonzalez-Herraez et al. (2005), we find

$$\frac{4v_{g,eff}}{L} = \frac{4v_g/L}{1 - \frac{1}{4} \frac{4v_g/L}{\Gamma_0} G} > \Gamma_+ = \Gamma_0(1 + G/4). \quad (\text{A.45})$$

This result shows that even with the changes in the phonon decay rate produced by the cooling dynamics, the requisite separation of timescales are still satisfied because the Brillouin nonlinearity produces a fast light effect for the participating anti-Stokes photons.

A.2 Pump-probe theory

In this section, we develop a mean-field theory to describe the pump-probe measurements. In these measurements, both pump and probe couple to the same phonon yielding the coupled envelope equations given by

$$\dot{a}_{aS} + \frac{\gamma}{2} a_{aS} = -igA_p b_{aS} \quad (\text{A.46})$$

$$\dot{a}_{sig} + \frac{\gamma}{2} a_{sig} = -igA_{pr} b_{aS} \quad (\text{A.47})$$

$$\dot{b}_{aS} + \frac{\Gamma_0}{2} b_{aS} = -iga_{aS} A_p^\dagger - iga_{sig} A_{pr}^\dagger + \bar{\xi}_{aS} \quad (\text{A.48})$$

where A_{aS} is the anti-Stokes light scattered from the pump A_p and A_{sig} is the anti-Stokes light scattered by the probe the undepleted probe laser A_{pr} .

In the quasistatic limit (i.e., $\gamma > \Gamma_0$) and assuming the $|A_p| \gg |A_{pr}|$, the effective phonon dynamics is given by Eq. (A.18) and the power spectrum of the scattered probe light is given by

$$\begin{aligned} S_{sig}[\omega, P_p] &\equiv \int_{-\infty}^{\infty} d\tau e^{i\omega\tau} \langle a_{sig}^\dagger(t+\tau) a_{sig}(t) \rangle \\ &= \frac{\Gamma_0 G_p L P_{pr}}{4v_g} \frac{\Gamma_0 n_{th}}{\Gamma_{aS}} \frac{\Gamma_{aS}}{\omega^2 + \Gamma_{aS}^2/4}. \end{aligned} \quad (\text{A.49})$$

where P_{pr} is the fixed probe power and Γ_{aS} is the phonon decay rate dependent upon the pump power defined in Eq. (2) of the main text. This result shows that as Γ_{aS} increases, i.e., with increased pump power, the power spectrum broadens and decreases in magnitude. To obtain the theoretical curve shown in Fig. 2c, we use the peak value of $S_{sig}[0, 0]$ to determine the constant prefactor in Eq. (A.49) where $\Gamma_{aS} \rightarrow \Gamma_0$, including the optical to radiofrequency conversion

$$S_{sig}[0, 0] = \frac{G_p L P_{pr}}{v_g} \frac{n_{th}}{\Gamma_0^2}. \quad (\text{A.50})$$

Moving out of the rotating frame yields the prediction for the scattered probe power spectrum is

$$S_{sig}^{RF}[\omega, P_p] = \frac{\Gamma_0^2/4}{(\omega - \omega_{pr} - \Omega)^2 + \Gamma_{aS}^2/4} S_{sig}^{RF}[0, 0], \quad (\text{A.51})$$

and used to plot the theory in Fig. 2e.

A.3 Brillouin gain simulations

We calculate the Brillouin gain spectrum by utilizing finite element simulations of the optical and acoustic modes of the liquid-core optical fiber (LCOF). By including empirically derived material properties (see Tab. A.1) and damping for silica Vacher et al. (1981) and CS₂ Coakley & Detenbeck (1975), these simulations yield the spatial mode profiles for the electric field \mathbf{E} and the elastic displacement \mathbf{u} (Fig. 1c & d). We obtain the Brillouin gain by evaluating the dissipated mechanical power using the equation

$$G_B = \frac{\omega_p}{\Omega} \frac{1}{P_p P_S} \int_{wg} d^2x \langle \mathbf{f} \cdot \dot{\mathbf{u}} \rangle \quad (\text{A.52})$$

where P_p and P_S are the respective pump and Stokes powers of the simulated electromagnetic fields, Ω is the angular frequency of the mechanical mode, \mathbf{f} is the electrostrictive force density, \int_{wg} is an integral over the waveguide cross-section, and $\langle \mathbf{A} \cdot \mathbf{B} \rangle$ is the time average of the vector product $\mathbf{A} \cdot \mathbf{B}$. For propagation

along the z-axis, the electrostrictive force density \mathbf{f} is given by

$$f_j = \frac{1}{2}\varepsilon_0 n^4 p_{ijkl} \partial_i (E_k E_l^*) \quad (\text{silica}) \quad (\text{A.53})$$

$$\mathbf{f} = -\frac{1}{4}\varepsilon_0 \gamma_e \nabla |\mathbf{E}|^2 \quad (\text{CS}_2) \quad (\text{A.54})$$

where ε_0 is the permittivity of vacuum, n is the refractive index, p_{ijkl} is the photoelastic tensor, γ_e is the electrostrictive constant, and the Einstein summation convention is assumed for repeated indices. In these expressions, we neglect the modal differences between the pump and the Stokes fields.

Acoustic dissipation critically determines the predicted power spectrum. We account for dissipation by including empirically obtained acoustic quality factors for silica and CS₂ in our simulations Coakley & Detenbeck (1975); Vacher et al. (1981). The parameters used in our simulation are summarized in the table below.

material	parameter	value
CS ₂	density	1260 kg/m ³
	refractive index	1.5885
	speed of sound	1226 m/s
	electrostrictive constant (γ_e)	2.297
	acoustic quality factor	23.5
SiO ₂	density	2203 kg/m ³
	refractive index	1.445
	Young's modulus	73.1 GPa
	shear modulus	31.24 GPa
	phot. elas. tensor (p_{11}, p_{12}, p_{44})	(0.125, 0.27, -0.073)
	acoustic quality factor	1800

Table A.1: Parameters used in simulations of spontaneous Brillouin scattering spectra.

References

- Abedin, K. S. 2005, Optics Express, 13, 10266
- Anderson, M. H., Ensher, J. R., Matthews, M. R., Wieman, C. E., & Cornell, E. A. 1995, science, 269, 198
- Ashkin, A. 1978, Physical Review Letters, 40, 729
- Aspelmeyer, M., Kippenberg, T. J., & Marquardt, F. 2014, Reviews of Modern Physics, 86, 1391
- Bahl, G., Tmes, M., Marquardt, F., & Carmon, T. 2012, Nature Physics, 8, 203
- Behunin, R. O., Otterstrom, N. T., Rakich, P. T., Gundavarapu, S., & Blumenthal, D. J. 2018, Physical Review A, 98, 023832
- Behunin, R. O., Ou, Y.-H., & Kieu, K. 2019, Physical Review A, 99, 063826
- Behunin, R. O., & Rakich, P. T. 2023, Physical Review A, 107, 023511
- Boyd, R. W. 2020, Nonlinear optics (Academic press)
- Chan, J., Alegre, T., Safavi-Naeini, A. H., et al. 2011, Nature, 478, 89
- Coakley, R. W., & Detenbeck, R. W. 1975, JOSA, 65, 6
- Davis, K. B., Mewes, M.-O., Andrews, M. R., et al. 1995, Physical review letters, 75, 3969
- Epstein, R. I., Buchwald, M. I., Edwards, B. C., Gosnell, T. R., & Mungan, C. E. 1995, Nature, 377, 500
- Gonzalez-Herraez, M., Song, K.-Y., & Thévenaz, L. 2005, Applied Physics Letters, 87
- Hänsch, T. W., & Schawlow, A. L. 1975, Optics Communications, 13, 68
- Hong, S., Riedinger, R., Marinković, I., et al. 2017, Science, 358, 203
- Kharel, P., Behunin, R. O., Renninger, W. H., & Rakich, P. T. 2016, Physical Review A, 93, 063806
- Kieu, K., Churin, D., Schneebeli, L., Norwood, R. A., & Peyghambarian, N. 2013, Optics letters, 38, 543
- Kieu, K., Churin, D., Wright, E., Norwood, R., & Peyghambarian, N. 2014, arXiv preprint arXiv:1402.7089
- Li, J., Lee, H., Chen, T., & Vahala, K. J. 2012, Optics express, 20, 20170
- Ludlow, A. D., Boyd, M. M., Ye, J., Peik, E., & Schmidt, P. O. 2015, Reviews of Modern Physics, 87, 637
- Marshall, W., Simon, C., Penrose, R., & Bouwmeester, D. 2003, Physical Review Letters, 91, 130401
- Okawachi, Y., Bigelow, M. S., Sharping, J. E., et al. 2005, Physical review letters, 94, 153902
- Otterstrom, N. T., Behunin, R. O., Kittlaus, E. A., & Rakich, P. T. 2018, Physical Review X, 8, 041034
- Phillips, W. D., & Metcalf, H. 1982, Physical Review Letters, 48, 596
- Sheik-Bahae, M., & Epstein, R. I. 2007, nature photonics, 1, 693
- Shelby, R., Levenson, M., Walls, D., Aspect, A., & Milburn, G. 1986, Physical Review A, 33, 4008

- Shin, H., Cox, J. A., Jarecki, R., et al. 2015, Nature communications, 6, 1
- Vacher, R., Pelous, J., Plicque, F., & Zarembowitch, A. 1981, Journal of Non-Crystalline Solids, 45, 397
- Wineland, D. J., Drullinger, R. E., & Walls, F. L. 1978, Physical Review Letters, 40, 1639
- Zhu, C., & Stiller, B. 2022, arXiv preprint arXiv:2208.06824